



AFRL-RX-WP-TP-2009-4135

**DIGITAL IMAGE CORRELATION OF Ni-BASE
SUPERALLOY RENÉ 88DT USING IN SITU SEM TENSION
EXPERIMENTS (PREPRINT)**

S. Fairchild, M.A. Tschopp, B.B. Bartha, T. Murray, and W.J. Porter

Metals Branch

Metals, Ceramics and NDE Division

NOVEMBER 2008

Approved for public release; distribution unlimited.

See additional restrictions described on inside pages

STINFO COPY

**AIR FORCE RESEARCH LABORATORY
MATERIALS AND MANUFACTURING DIRECTORATE
WRIGHT-PATTERSON AIR FORCE BASE, OH 45433-7750
AIR FORCE MATERIEL COMMAND
UNITED STATES AIR FORCE**

REPORT DOCUMENTATION PAGE					Form Approved OMB No. 0704-0188	
<p>The public reporting burden for this collection of information is estimated to average 1 hour per response, including the time for reviewing instructions, searching existing data sources, gathering and maintaining the data needed, and completing and reviewing the collection of information. Send comments regarding this burden estimate or any other aspect of this collection of information, including suggestions for reducing this burden, to Department of Defense, Washington Headquarters Services, Directorate for Information Operations and Reports (0704-0188), 1215 Jefferson Davis Highway, Suite 1204, Arlington, VA 22202-4302. Respondents should be aware that notwithstanding any other provision of law, no person shall be subject to any penalty for failing to comply with a collection of information if it does not display a currently valid OMB control number. PLEASE DO NOT RETURN YOUR FORM TO THE ABOVE ADDRESS.</p>						
1. REPORT DATE (DD-MM-YY) November 2008		2. REPORT TYPE Journal Article Preprint		3. DATES COVERED (From - To) 01 November 2008 – 01 November 2008		
4. TITLE AND SUBTITLE DIGITAL IMAGE CORRELATION OF Ni-BASE SUPERALLOY RENÉ 88DT USING IN SITU SEM TENSION EXPERIMENTS (PREPRINT)				5a. CONTRACT NUMBER In-house		
				5b. GRANT NUMBER		
				5c. PROGRAM ELEMENT NUMBER 62102F		
6. AUTHOR(S) S. Fairchild (AFRL/RXLMN) M.A. Tschopp (Universal Technology Corporation) B.B. Bartha (United Space Alliance) T. Murray and W.J. Porter (University of Dayton Research Institute)				5d. PROJECT NUMBER 4347		
				5e. TASK NUMBER RG		
				5f. WORK UNIT NUMBER M02R3000		
7. PERFORMING ORGANIZATION NAME(S) AND ADDRESS(ES) Metals Branch (RXLMN) Metals, Ceramics and NDE Division Materials and Manufacturing Directorate Wright-Patterson Air Force Base, OH 45433-7750 Air Force Materiel Command, United States Air Force				8. PERFORMING ORGANIZATION REPORT NUMBER AFRL-RX-WP-TP-2009-4135		
9. SPONSORING/MONITORING AGENCY NAME(S) AND ADDRESS(ES) Air Force Research Laboratory Materials and Manufacturing Directorate Wright-Patterson Air Force Base, OH 45433-7750 Air Force Materiel Command United States Air Force				10. SPONSORING/MONITORING AGENCY ACRONYM(S) AFRL/RXLMN		
				11. SPONSORING/MONITORING AGENCY REPORT NUMBER(S) AFRL-RX-WP-TP-2009-4135		
12. DISTRIBUTION/AVAILABILITY STATEMENT Approved for public release; distribution unlimited.						
13. SUPPLEMENTARY NOTES To be submitted to Scripta Materialia PAO Case Number and clearance date: 88ABW-2008-0923, 12 November 2008. The U.S. Government is joint author of this work and has the right to use, modify, reproduce, release, perform, display, or disclose the work.						
14. ABSTRACT Digital image correlation was used to obtain the strain behavior of a polycrystalline nickel-based superalloy, René 88DT, from an in situ scanning electron microscope tensile experiment at room temperature. A subsequent correlation with crystal orientations shows that the average maximum principal strain tends to increase with increasing Schmid factor. The range of the extreme values for the maximum principal strain also increases closer to the grain boundary, signifying that grain boundaries and triple junctions initiate plasticity within polycrystalline René 88DT.						
15. SUBJECT TERMS Nickel-based superalloy, in situ SEM, digital image correlation, plasticity						
16. SECURITY CLASSIFICATION OF:			17. LIMITATION OF ABSTRACT: SAR	18. NUMBER OF PAGES 18	19a. NAME OF RESPONSIBLE PERSON (Monitor) James M. Larsen	
a. REPORT Unclassified	b. ABSTRACT Unclassified	c. THIS PAGE Unclassified			19b. TELEPHONE NUMBER (Include Area Code) N/A	

Digital Image Correlation of Ni-base superalloy René 88DT using in-situ SEM tension experiments

M.A. Tschopp^a, B.B. Bartha^b, S. Fairchild^c, T. Murray^d, W.J. Porter^d

^a Universal Technology Corporation
Dayton, OH 45433

^b United Space Alliance
Cape Canaveral AFB, FL 32815

^c Air Force Research Laboratory
Wright Patterson AFB, OH 45433

^d University of Dayton Research Institute
Dayton, OH 45431

Digital image correlation was used to obtain the strain behavior of a polycrystalline nickel-based superalloy, René 88DT, from an *in situ* scanning electron microscope tensile experiment at room temperature. A subsequent correlation with crystal orientations shows that the average maximum principal strain tends to increase with increasing Schmid factor. The range of the extreme values for the maximum principal strain also increases closer to the grain boundary, signifying that grain boundaries and triple junctions initiate plasticity within polycrystalline René 88DT.

Nickel-based superalloy; in situ SEM; Digital image correlation; Plasticity

Fatigue variability plays a crucial role in determining the total life of fracture critical turbine engine components. The Air Force's Engine Rotor Life Extension and Materials Damage Prognosis programs have examined life-limiting factors in an effort to extend the lives of service components. Various material specific mechanisms contribute to fatigue variability (1). For example, fatigue variability has been associated competing failure mechanisms in Ti-6246, René 88DT and IN-100 (2-3). The ability to predict fatigue variability and the minimum life of critical components significantly affects the sustainability of an aircraft fleet.

To accurately predict fatigue variability, it is vital to understand what the fatigue-critical microstructural features are and exactly how these may couple with loads and temperatures to nucleate damage in these critical components. It is a commonly held notion that damage nucleates in locations of large strain concentrations or where substantial inelastic deformation exists. Digital image correlation (DIC) is a technique often used to investigate how strain localizes around part geometric features, such as cracks, holes, and notches. Recently, this technique has been applied at increasingly smaller scales, i.e., *in situ* SEM (4-7) and AFM (8-9) studies are now on the order of the underlying microstructural features. Similar *in situ* studies are also used to understand how microstructure evolves with deformation (e.g., in Ti alloys 10-11). The ability to combine these studies and understand how specific microstructure features evolve and couple with local strains with can greatly enhance our ability to predict fatigue and, perhaps, engineer better materials for fatigue.

In this paper, we present an *in situ* SEM technique that can be used to obtain the local deformation behavior of polycrystalline Ni-based superalloys at room and elevated temperatures.

René 88DT, a forged polycrystalline Ni-based superalloy used in aircraft engine components, was chosen as a novel material for this work. Results correlate the local strain behavior and (from DIC) with the grain orientations and grain boundary character (from OIM). Ultimately, the objective of this research is to understand how the microstructural variability of polycrystalline materials influences fatigue variability. This study was conducted at room temperature; however, future work aims to examine this behavior at high temperatures.

The experimental setup consisted of a screw-driven 1000 lb tensile stage (Ernest F. Fullam, Inc., Fig. 1) placed inside a Quanta 600 FEG SEM. The tensile specimen was a flat dog-bone-shaped specimen with gage dimensions of 3 mm wide x 1 mm thick x 10 mm long.

Digital image correlation often uses a speckle pattern to track displacements. Here, we coat the specimen surface with Pt nanoparticles using a laser ablation process termed **through thin film ablation** (TTFA) (12). The specimen surfaces were mechanically polished to a 1 μm finish prior to deposition; a clean polished surface is essential for optimal imaging and deposition. The TTFA technique used a 10nm Pt thin film deposited onto a fused silica plate transparent to the laser wavelength (wavelength = 248nm, energy density = 0.5 J/cm²). The chamber was filled with Ar at a pressure of 5 torr. The laser irradiates the Pt thin film from the backside, propelling Pt nanoparticles at the intended target, i.e., in this case, the tensile specimen. The high density of the Pt nanoparticles compared to the René 88DT provided sufficient contrast in the secondary electron images for digital image correlation. The TTFA nanoparticles are deposited in a random non-agglomerated speckle pattern that allows sub-pixel resolution of displacement. Platinum nanoparticles enable DIC at higher temperatures than gold patterns (e.g., Ref. 4), i.e.,

into the temperature range where nickel-based superalloys are typically used. Similar nanoparticle speckle patterns have also been applied to surfaces through spin-casting (13-14) or lithography techniques (15).

Each tensile specimen was then mounted into the tensile stage grip fixture and preloaded to allow the specimen to seat and to mitigate specimen rotation. Both secondary electron (SE) and backscatter electron (BSE) images were collected at 16 bit depth at a pixel resolution of 4096 by 3773 pixels. The SE images were used for digital image correlation while the BSE images provided sufficient detail for aligning the in-situ images with post-processed OIM images. At each load step, the stage controller was turned off while acquiring the images to minimize any potential distortion effects due to the motor operating the stage. Each image was focused by raising and lowering the stage fixture to keep the same working distance; this minimizes any additional artifacts due to focusing with the beam only.

The tensile specimen was loaded in 12 steps to 1234 MPa (yield regime) with larger (smaller) step sizes in the elastic (plastic) regime. After unloading the specimen, the Pt nanoparticles were removed from the surface and OIM was used to measure the crystallographic orientations of the underlying microstructure. Digital Image Correlation was performed on each image with ViC-2D to calculate the displacement field for each load increment. The image at the 0MPa unloaded condition was used as a reference image for the displacement calculation. A subset size of 99 pixels was used for each calculation with a 5 pixel step size and cubic B-spline interpolation. The displacement maps were then converted to principal strain maps for the remainder of the analysis.

Figure 1 shows the result of digital image correlation for a nominal stress of 1144 MPa. Fig. 1(a) shows the reference image, while Fig. 1(b) shows the deformed image with evidence of slip bands in some grains; the loading axis is horizontal. The digital image correlation software uses Fourier transforms of multiple subsets of these images to calculate the sub-pixel displacements and strains, as shown in Fig. 1(c). The average maximum principal strain for the 274 μm by 230 μm region of interest is 0.026. The high strain concentrations are localized in bands oriented approximately 45 degrees from the tensile direction, as would be expected. The bands present in Fig. 1(c) do not necessarily correlate with the observed slip bands in Fig. 1(b); grain boundaries also play an important role in the high maximum principal strain bands.

Further analysis requires the principal strain maps to overlap the crystallographic information obtained from the OIM scan. By aligning the inverse pole figure in Figure 2(a) with the BSE image in Figure 2(b), the strain maps can be correlated with information obtained from crystal orientations, e.g., Schmid factor, Taylor factor, etc. The image quality (IQ) map (Fig. 2c) is a quantitative measure of the fit of the Kikuchi pattern from the OIM scan. The grain boundaries have a lower IQ value than the grain interiors, which allows for a better alignment with the BSE image. The IQ map image is then aligned with the BSE image through rotation, translation, and rescaling, as shown in Figure 2(d). However, the pixels and their spacing may still be different between the two datasets. Therefore, a nearest neighbor interpolation is used to match the pixels in the IQ map with the pixels in the BSE image. All subsequent analyses are related to correlating the strain behavior in Figure 1 with quantitative information relating to the crystallographic grain orientation.

Figure 3 shows the correlation between the Schmid factor and the maximum principal strain. Each data point represents 1 pixel from the strain map of Figure 1, i.e., over 460,000 data points total. Figure 3(a) shows the distribution of Schmid factors within the René 88DT grain structure over the same area as Fig. 1(c). The Schmid factor resolves the tensile stress onto the $\{111\}$ slip plane in the $\langle 110 \rangle$ slip direction, i.e., a higher Schmid factor should coincide with a higher stress in the direction of slip. Fig. 3(b) shows the relation between the maximum principal strain and the Schmid factor. At low Schmid factors, the range of the extreme values of maximum principal strain (i.e., the low and high values) is not as large as for higher Schmid factors. There appears to be no decisive relationship between the Schmid factor and extreme values of the maximum principal strain, since very high maximum principal strains are observed in regions with Schmid factors of approximately 0.35. The high extreme values of maximum principal strain are of particular interest because of their potential association with how damage initiates under fatigue conditions. The average maximum principal strain also shows an increasing trend in maximum principal strain with increasing Schmid factor. These trends may not be as strong because the strain localization after yield is not merely a function of the crystallographic orientation of the underlying lattice, but may also depend on the grain boundary structure, triple junctions, the grain size, and the neighboring grains.

The grain boundary network may also be associated with the localization in strain within the region of interest. Figure 5 shows the correlation between the distance from the grain boundary and the maximum principal strain. The grain boundary pixels were identified by determining if there were two or more grains present in adjacent pixels (4-neighborhood). Fig. 5(a) shows the

maximum principal strain map with the grain boundary pixels in black. The distance from the boundary was calculated using a Euclidean distance transform. Interestingly, Fig. 5(b) shows that the upper (lower) extreme values for maximum principal strain decreases (increases) as the distance from the grain boundary increases. This indicates that the grain boundary has a greater propensity to accommodate strain than the grain interiors --- both lower and higher strains. The strain behavior at large distances from the boundary is related to the few large grains within the region of interest. The strain behavior at intermediate distances from the GB encompasses a large number of grains, yet the strain range is not as large as at the boundary. The average strain behavior is equivalent for the first 6 μm from the boundary; the deviation at larger distances is affected by the few large grains. These results indicate that strains are much more likely to localize at high values at the grain boundary regions rather than the grain interiors.

Since the grain boundary region has been segmented from the grain interior regions, an extension is to examine the correlation between strain localization and grain boundary character. Graphs similar to Figs. 3 and 4 were plotted to compare the minimum misorientation angle (i.e., taking into account symmetry) with the maximum principal strain. However, the maximal principal strain did not trend with respect to grain boundary misorientation angle. On average, there was more variation at lower disorientation angles; however, this may be related to the lower number of low angle boundaries in the region of interest, as the distribution of boundaries follows the MacKenzie distribution. Additional plots comparing the maximum principal strain to the grain boundary orientation with respect to the loading axis also shows little correlation in this study. A larger subset of boundaries may be needed to correlate local strains with specific grain boundary

character. Additionally, the influence of grain boundary plane inclination and triple junctions may be important for local straining as well.

In summary, we present a novel methodology for preparing tensile specimens for *in situ* SEM digital image correlation (DIC) through a laser ablation process, through thin film ablation. By combining deformation strain maps from DIC with orientation imaging microscopy (OIM) data, the correlation between the maximum principal strain and a number of microstructure-dependent parameters can be ascertained, e.g., Schmid factor (Fig. 3) and distance from grain boundary (Fig. 4) in this analysis.

On average, we find that the maximum principal strain tends to increase with increasing Schmid factor. The range of the extreme values for the maximum principal strain also increases closer to the grain boundary, signifying that grain boundaries and triple junctions initiate plasticity within polycrystalline René 88DT. Correlating the strain localization to specific boundaries was not observed in this study.

This analysis shows that the strain localization in polycrystalline superalloys, which is important to plasticity, fatigue, and fracture, is a combination of a number of factors related to grain orientation and the grain boundary network. This will require coupling between further experiments and computational approaches to fully understand, and is vital to understanding how damage nucleates in fatigue-critical polycrystalline components. Furthermore, results of this ilk may also be used to estimate constitutive parameters with inverse computational methods based on full-field measurements (cf. 16-17).

This work was performed at the Air Force Research Laboratory, Materials and Manufacturing Directorate, AFRL/RXLMN, Wright-Patterson Air Force Base, OH. The financial support of the Air Force Office of Scientific Research (AFOSR) through the AFOSR task no. 92ML02COR with Dr. Victor Giurgiutiu as the program manager is gratefully acknowledged. The authors acknowledge the Material Characterization Facility at the AFRL for their help in this work.

- [1] S.K. Jha, M.J. Caton, J.M. Larsen, *MSE A* 468–470 (2007) 23–32.
- [2] S.K. Jha, J.M. Larsen *JOM* Sept 2005 50-54.
- [3] S.K. Jha, M.J. Caton, J.M. Larsen, *Superalloys* 2008, 565-572.
- [4] M.A. Sutton et al., *Experimental Mech.* 47 (2007) 775-788.
- [5] M.A. Sutton et al., *Experimental Mech.* 47 (2007) 789-804.
- [6] A. Soula et al., *Superalloys* 2008, 387-394.
- [7] J. Kang, Y. Ososkov et al., *Scr Mater* 56 (2007) 999-1002.
- [8] W.G. Knauss, I. Chasiotis et al., *Mech of Mater* 35 (2003) 217-231.
- [9] I. Chasiotis, W.G. Knauss, *Experimental Mech.* 42 (2002) 51-57.
- [10] C.J. Boehlert, C.J. Cowen et al, *Scripta Mat.* 55 (2006) 465-468.
- [11] C.J. Cowen, C.J. Boehlert, *Met Trans A* 38A (2007) 26-.
- [12] P.T. Murray, E. Shin, *Mater. Lett.* 62 (2008) 4336-4338.
- [13] T.A. Berfield, J.K. Patel et al., *Small* 2 (2006) 631-635.
- [14] T.A. Berfield, J.K. Patel et al., *Experimental Mech.* 47 (2007) 51-62.
- [15] W.A. Scrivens, Y. Luo et al., *Experimental Mech.* 47 (2007) 63-77.
- [16] S. Avril, et al., *Experimental Mechanics* 48 (2008) 381-402.
- [17] T. Hoc, J. Crépin et al., *Acta Mater* 51 (2003) 5477-5488.

Figure Captions

Figure 1. (a,b) SE images of René 88DT with nanoparticles at no load and after yield. (c) Digital image correlation was used to generate the principal strains within this region.

Figure 2. Image alignment process: (a) Inverse pole figure showing crystal orientations from OIM scan, (b) BSE image of René 88DT prior to deformation, (c) IQ map of microstructure, and (d) aligned images.

Figure 3. Graph showing the correlation between the Schmid factor and the maximum principal strain at a nominal stress of 1144 MPa.

Figure 4. Graph showing the correlation between the distance from the grain boundary and the maximum principal strain.

Figure 1

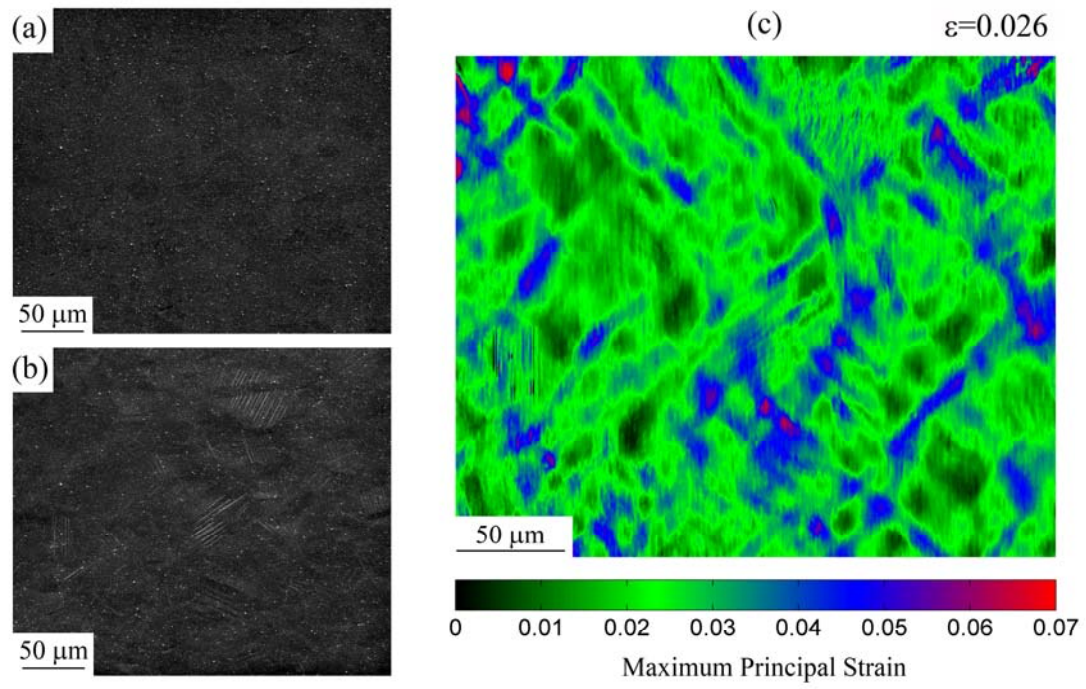


Figure 2

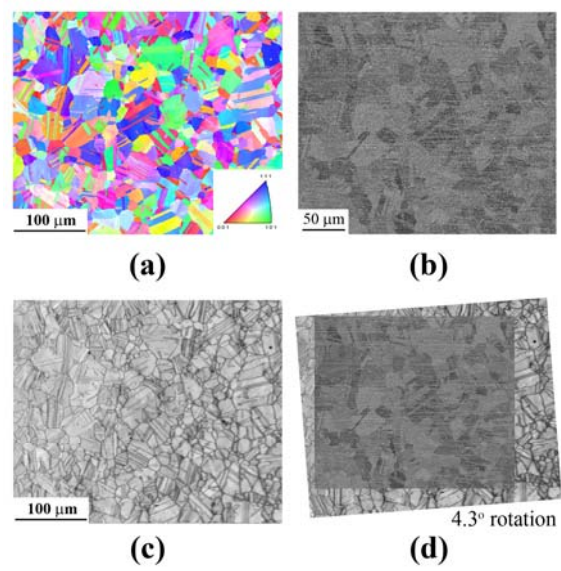


Figure 3

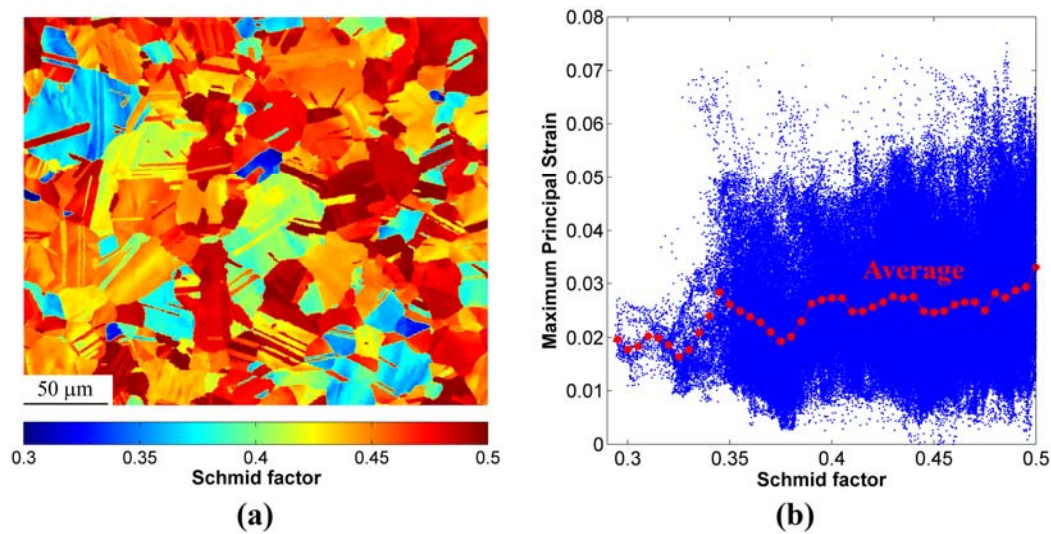


Figure 4

